Imaging the interactions of chimeric antigen receptor-expressing T-cells with colorectal cancer cells

Debasis Banik[1], Christopher Ward[2], Ziwei Zhang[1], Daniel Heraghty[1], Prasanna Suresh[1], Bing Li[1], Shekhar Kedia[1], Simon J. Davis[3,4], James P. Roy[5], Michael A. Chapman[5,6,7], Bidesh Mahata[2*], David Klenerman[1*]

[1]Yusuf Hamied Department of Chemistry, University of Cambridge, Cambridge, CB2 1EW, UK.

[2]Department of Pathology, University of Cambridge, Cambridge, CB2 1QP, UK.

[3]Radcliffe Department of Medicine, John Radcliffe Hospital, University of Oxford, Oxford OX3 9DS, UK.

[4]Medical Research Council Human Immunology Unit, John Radcliffe Hospital, University of Oxford, Oxford OX3 9DS, UK.

[5]MRC Toxicology Unit, University of Cambridge, Cambridge, UK.

[6]Department of Haematology, University of Cambridge, Cambridge, UK.

[7]Addenbrooke's Hospital, Cambridge Universities Foundation Trust, Cambridge, UK.

*Correspondence e-mail: dk10012@cam.ac.uk & bm562@cam.ac.uk

ABSTRACT

Chimeric antigen receptor (CAR) T-cell therapy has shown unprecedented success in haematological cancers but faces challenges in solid tumours. Although carcinoembryonic antigen-related cell adhesion molecule 5 (CEACAM5) is differentially expressed in many solid tumours, CEACAM5 CAR T-cells are ineffective. Here, we have studied the interaction of CEACAM5 targeting CAR primary T-cells with colorectal cancer (CRC) cells using fluorescence microscopy. We find that CRC cells' glycocalyx is much thicker than the CAR T-cell and likely contributes to immune-escape. Oscillating calcium flux, a signature of non-sustained triggering and decreased killing, was observed when CAR T-cells interacted with CRC, which increased with increasing cell-seeding time. This was because CEACAM5 became increasingly unavailable on the CRC cell monolayer, as revealed by fluorescence imaging. Local proteolytic treatment with trypsin to disrupt the CRC cell monolayer, using a micropipette, increased CEACAM5 availability, decreased glycocalyx thickness, and restored sustained CAR T-cell calcium fluxes, increasing the killing of CRC cells. Our results reveal why CAR T-cells targeting CEACAM5 are ineffective and suggest possible routes for improved therapy.

One Sentence Summary

CEACAM5 unavailability and the thick CRC cell glycocalyx are major barriers to CAR T-cells, which local proteolysis helps to overcome.

INTRODUCTION

T-cells are an essential part of the adaptive immune system. Each T-cell expresses T-cell receptors (TCRs) which recognise peptide major histocompatibility complexes (pMHCs) on the surface of antigen presenting cells (APCs). In contrast, synthetically designed chimeric antigen receptors (CARs) originally comprised target-binding single chain variable fragments (scFvs) connected to an intracellular signaling domain, CD3ζ via a transmembrane region. Additional signaling domains, i.e., from CD28 and 4-1BB contribute to later generations of CARs. Recently, CAR T-cell therapy has been approved by the United States Food and Drug Administration (FDA) for the treatment of B-cell acute lymphoblastic leukemia (ALL), with several products now in use in the clinic (*1-4*). However, the same therapy is ineffective in solid tumours, including colorectal cancer (CRC) (*5-8*). CRC, the third most common global cancer, is responsible for ~ 10 % of total cancer incidences and deaths in 2020, with ~ 30 months of median overall survival (mOS) for metastatic CRC (mCRC) patients (*9*).

Understanding CAR T-cells' functions and limitations are essential for generating better therapeutic designs in the future. CAR T-cells require higher antigen concentration than wild-type T-cells for activation (*10*). Lck independent CAR T-cell activation was shown to be driven by the CD28 signaling domain and the SRC family kinase Fyn (*11*), leading to the formation of a non-classical and potent immunological synapse generating rapid cytotoxicity (*12*). Recently, Xiao et al. showed that the exclusion of large phosphatase CD45 at the CD19 CAR T-cell/Raji B-cell interface, used as a model system, is intrinsic to CAR T-cell activation, likely due to favouring net CAR phosphorylation by kinases, as proposed by the 'kinetic-segregation' model (*13, 14*).

Carcinoembryonic antigen-related cell adhesion molecule 5 (CEACAM5) overexpressed in many cancer types including lung, pancreatic tumours, and by CRC. There has not been much

progress treating these tumours with CAR T-cells for multiple reasons, such as poor accessibility of the cancer cells to the CAR T-cells, poor persistence of the CAR T-cells, and organ toxicity (*15*). Here, we investigate the CAR T-cell/CEACAM5^{+} CRC interaction in vitro to elucidate mechanistic details using imaging methods that we have developed to study the early events of T-cell activation (*16*). We observed that the thick glycocalyx of CRC cell and unavailability of CEACAM5 on CRC cell monolayers play crucial roles in reducing CAR T-cell/CRC interactions. We observed enhanced interaction and killing of CRC cells when we locally treated the CRC cells' monolayers with a proteolytic enzyme, trypsin. Our results suggest ways in which CAR T-cell based CRC therapy could be made more effective.

RESULTS

Early-stage monitoring of CEACAM5 CAR T-cell/CRC interaction

Jurkat and primary human T-cell derived CEACAM5 CAR T-cells and CRC cells (LS-174T, LS-1034 & RKO) were prepared (see Materials and Methods; Fig. S1-S3). Fig. 1 shows early-stage imaging of the CEACAM5 CAR T-cell/CRC cell interaction using brightfield and epifluorescence calcium imaging. Firstly, we tested the CEACAM5 sensitivity of CAR-expressing Jurkat T-cells employing our "second generation" supported lipid-bilayer system (SLB2), which presents ligands for the small and large adhesion proteins CD2 (i.e., CD58) and LFA-1 (i.e., ICAM-1), alongside the major antigen presenting cell (APC) glycocalyx elements, CD43 and CD45 (~ 40 nm in length), human CEACAM5/CD66e protein as an antigen for the CAR T-cell, and gp100-MHC, an irrelevant peptide-MHC used to block free nickellated lipids (see Materials and Methods).

We prepared CEACAM5 expressing (CEACAM5^{+}) and CEACAM5 non-expressing (CEACAM5^{-}) SLB2s. CAR T-cells labelled with Fluo-4-AM (a calcium indicator) and CellMask Deep Red (a plasma membrane stain) were then allowed to interact with the SLB2s.

We observed that CAR T-cells formed close contacts by excluding CD45/CD43 on the bilayer with stable cell footprint and produced robust calcium fluxes on the CEACAM5^{+} SLB2s. On CEACAM5^{-} (control) SLB2s, unstable close contacts along with moving cell footprints were observed, and no calcium fluxes were produced (Movie S1). This result shows that CAR T-cells are highly sensitive to the presence of human CEACAM5 protein. Interestingly, we observed 40 % average exclusion of CD45/CD43 by CAR T-cells (Fig. S4), similar to wild-type Jurkat and primary T-cells in our previous study (*16*), suggesting similar interactions with the SLB2 system.

LS-174T and RKO are two well-known CEACAM5^{+} and CEACAM5^{-} CRC cell lines, respectively, which we choose for our experiments. We sought to mimic tumour growth-related changes by plating out CRC cells for 24 and 48 hours (hrs). Fig. 1A shows the experimental scheme for our cell-cell assay wherein Fluo-4-AM pre-labelled CAR T-cells interact with the LS-174T monolayer and produce calcium fluxes. Noting the off-target respiratory distress experienced by colon cancer patients within 15 minutes of CAR T-cell infusion (*17*), we decided to focus on the first one hour of CAR T-cell/LS-174T interaction using simultaneous measurement of calcium fluxes and brightfield images.

Firstly, we monitored the interaction using a 20X objective lens and found that the Jurkat CAR T-cells gave sustained calcium fluxes (red arrows in Movie S2) with early seeding LS-174T monolayer (24 hrs, denoted by pink), whereas, no sustained flux was observed with longer seeding (48 hrs, denoted by blue). Delayed triggering of CAR T-cells was found on early seeded LS-174T monolayer compared to the SLB2 (Fig. S5). We repeated the same experiment with LS-1034, another CEACAM5^{+} CRC cell line, and found almost no triggering even at early seeding condition (Movie S3).

To investigate signaling on LS-174T monolayers in more details, we used a 60X objective lens and a CEACAM5$^-$ CRC cell line, RKO, as a control. CAR accumulation was observed as bright puncta formation during interaction with early seeded LS-174T monolayer (Movie S4). Brightfield images of LS-174T and the RKO monolayer (24 hrs, denoted by olive) interacting with CAR Jurkat T cells are shown in Fig. 1B. Representative calcium flux traces are shown in Fig. 1C and we have provided two Movies S5-S6. These results indicated that the increased and sustained calcium flux changed to oscillatory flux with increasing seeding time. Interestingly, similar oscillatory calcium fluxes were also observed on the RKO monolayer. Fig. 1B (3rd row; see red arrows) and Movie S7 reveals extensive killing of early seeded LS-174T cells by primary CAR T-cells. In contrast, within the first one hour of monitoring no killing was observed for longer seeded LS-174T and control monolayers. We present more calcium flux Movies S8-S9 to support our observations. We analysed the calcium flux traces shown in Fig. 1C, 1D and determined the residuals (Fig. S6-S7) and the upper and lower envelopes (Fig. S8). The results indicate that the oscillation amplitude increases on going from early to longer seeded LS-174T and the latter condition is very close to the control monolayer.

In summary, whereas CAR T-cells responded on early seeded LS-174T monolayers, decreased activation was observed with increasing seeding time. Therefore, our results show that CEACAM5$^+$ CAR T-cells are ineffective against CRC, in line with clinical observations (*15*).

The glycocalyces of CEACAM5-reactive CAR T-cells and LS-174T cells

There is a coating on the surface of all cells that has a critical role in modulating cell adhesion and controlling cell-cell interactions, called the glycocalyx. The glycocalyx comprises dense arrays of negatively charged, heavily glycosylated proteins and polysaccharides, the most important consequence of which is that it forms a physical barrier to cell contact (*18*). In cancer cells the glycocalyx increases in height, making it more difficult for T-cells to kill cancerous

tissue, especially solid tumours (*19, 20*). Therefore, it was interesting to test whether the reduced CAR T-cell/LS-174T interaction is associated with the presence of a thick glycocalyx on the tumour cell.

To measure the glycocalyx, CAR T-cells and early, longer seeded LS-174T cells were fixed and labelled with HMSiR-conjugated wheat germ agglutin (WGA-HMSiR; see Materials and Methods). WGA binds to the N-acetylglucosamine residues of the glycocalyx. We measured the glycocalyx thickness using resPAINT super-resolution (SR) imaging (*21*). Fig. 2A-F show 2D SR images of T-cell and LS-174T glycocalyces, which are ~ 100 nm and ~ 400 nm in thickness, respectively. However, no variation in thickness was observed for early and longer seeded LS-174T cells (Fig. 2G), so this could not be the explanation for the difference in CAR T-cell reactivity that we observed in the early and longer seeded cultures.

CEACAM5 sequestration as explanation for decreased CEACAM5 CAR T-cell/CRC interactions

To explain the decrease in CAR T-cell/LS-174T reactivity with increasing seeding time, we performed antigen mapping on the LS-174T monolayer using fluorescently labelled anti-CEACAM5 antibody. Fig. 3A (2nd row) shows a heterogeneous distribution of CEACAM5 on the early seeded monolayer is commonly observed for solid tumour antigens. Interestingly, on longer seeded monolayer CEACAM5 becomes increasingly unavailable, and the staining pattern matches that of RKO (Fig. 3A; 3rd & 4th row). This finding is also supported by an increase in the T-cell mean speed and track straightness on longer seeded LS-174T monolayers compared to the early seeded condition (Fig. S9 & Movie S10). After observing this, we imaged the CEACAM5 distribution on LS-174T cells after just 4 hrs seeding and found that CEACAM5 is available to almost all of the cells (Fig. 3A; top row). We concluded that the

unavailability in CEACAM5 on longer seeded LS-174T and RKO monolayers is the cause of the oscillating calcium fluxes characteristic of non-sustained triggering.

CD19 is a well-known target antigen used for CAR T-cell therapy in B-cell ALL patients. We wondered whether $CD19^+$ LS-174T will exhibit comparable antigen unavailability. We expressed CD19 on LS-174T cells (Fig. S10) and seeded these cells for 24 and 48 hrs. Imaging with fluorescently labelled anti-CD19 antibody revealed homogeneous expression of CD19 under both early and longer seeded conditions (Fig. 3A; two bottom rows). Calcium flux measurements in Jurkat CD19 CAR T-cells (Fig. S1C) interacting with longer seeded $CD19^+$ LS-174T reveal strong triggering (Fig. S11). Interestingly, LS-174T cells also express human epidermal growth factor receptor 2 (HER2) and we observed homogeneous expression of HER2 on early and longer seeded LS-174T monolayers using fluorescent anti-HER2 antibody (Fig. S12-13). Therefore, the antigen unavailability observed for CEACAM5, does not occur for CD19 and HER2.

Next, we sought to measure calcium flux and cytotoxic granules release for primary CAR T-cells when interacting with early seeded LS-174T monolayers. By labeling T-cells with Fluo-4-AM and lysotracker red, we observed increased calcium fluxes (~15 mins after CAR T addition) preceding the recruitment of granules (~40-50 mins) at the immunological synapse (IS) formed by the CAR T-cells with LS-174T cells (Fig. 3B & Movie S11). We analysed the granules' recruitment trajectories (Fig. 3C-D & Movie S12) and found the mean speed of recruitment varies between 0.005 to 0.04 μm/sec. Davenport et al. did similar analyses of primary CAR T-cells targeting HER2 and found granule recruitment speeds of ~ 0.10 μm/sec (*12*). This suggests that granule recruitment speed is target antigen dependent. We also observed that immediately after killing a LS-174T cell by releasing granules, the same primary CAR T-cell moved to another target (Movie S13), consistent with CAR T-cells acting as serial killers.

After observing CD45/CD43 exclusion on the SLB2 (Movie S1), we sought to image the same phenomenon at the CAR T-cell/tumour cell interface. Early seeded LS-174T monolayers and Jurkat CAR T-cells were labelled separately with anti-epithelial cell adhesion molecule (EpCAM) antibody-Alexa 647 and Gap8.3-Alexa 488 (anti-CD45 antibody) conjugates, respectively, and then allowed to interact for 30 mins. Fig. 3E shows late stage CD45 exclusion on T-cells (white arrow) at the CAR T-cell/LS-174T interface using a home-built epifluorescence selective plane illumination microscope (eSPIM) (see Materials and Methods).

Improving the CEACAM5 CAR T-cell/CRC interaction

Close inspection of CEACAM5 mapping on early seeded LS-174T monolayers revealed that CEACAM5 is located mostly at the intercellular junction (Fig. S14) and eventually disappears for longer seeded cells. A previous study showed that carcinoembryonic antigen (CEA) functions as an intercellular adhesion molecule for human colon carcinoma cell lines (*22*). We assumed that, with increased seeding time, LS-174T cells utilize CEACAM5 (a member of the CEA family) for adhesion at cell-cell junctions, making it unavailable to T-cells. This could be a potential mechanism for immune escape for CRC in the setting of CEACAM5 targeting CAR T-cell immunotherapy. Therefore, we conceived the idea of treating longer seeded LS-174T monolayers with the dissociating enzyme trypsin, making the CEACAM5 re-available.

Fig. 4A shows the experimental scheme for local trypsin treatment using a micropipette followed by calcium imaging of CAR T-cells on the trypsin treated longer seeded LS-174T monolayer. Movie S14 shows trypsin delivery to detach LS-174T cells from each other. To avoid any CAR T-cell/glass interactions after trypsin treatment, we choose fields of view (FOVs) where some LS-174T cells (i.e., the 2nd layer) could be seen above the monolayer. CEACAM5 mapping of similar FOVs is shown in Fig. S15. By choosing these FOVs, we could dissociate intercellular junctions in the 2nd layer as well as between the 2nd layer and monolayer

without significantly affecting the underlying monolayer. Immediately after trypsin treatment, we delivered Fluo-4-AM pre-labelled CAR T-cells onto the LS-174T monolayer and observed sustained increased calcium flux comparable to those seen for the early seeding condition (orange graphs of Fig. 4B, 4C). In control experiments, the RKO monolayer was treated with trypsin and we observed oscillatory calcium fluxes (olive graphs of Fig. 4B, 4C). Head-to-head comparison of calcium fluxes before and after trypsin treatment is shown in Fig. 4D and Movies S15-16. Interestingly, increased killing of LS-174T cells by primary CAR T-cells was observed within one hour on trypsin-treated monolayer (Movie S17).

After observing this improved CAR T-cell/LS-174T interaction, we confirmed that CEACAM5 became re-available on the trypsin treated LS-174T monolayer (Fig. 4E). First, CEACAM5s were imaged on longer seeded LS-174T monolayer using anti-CEACAM5 antibody labelling (Fig. 4E, top row). Following this, trypsin was used to dissociate the intercellular junctions and then anti-CEACAM5 antibody delivered using another micropipette. After antibody addition we waited for 20 mins so that unbound antibody could diffuse away. Interestingly, we found that CEACAM5 became increasingly re-available at the intercellular junction, to the extent observed for the early seeded condition (Fig. 4E, 2nd to 4th row). The results confirmed that locally treating cells with dissociative enzyme significantly increased the effectiveness of CAR T-cell/LS-174T interactions.

Next, we sought to determine the effect of trypsin on the LS-174T glycocalyx. Longer seeded LS-174T cells were treated with trypsin in bulk and fixed before resPAINT SR imaging. We observed a significant reduction of glycocalyx thickness in the presence of trypsin (Fig. 4F), as expected and in accordance with previous literature (*23*). In addition, the glycocalyx took on a “patchy” appearance.

We also tested trypsin treatment of early seeded LS-174T monolayers and observed faster triggering of Jurkat CAR T-cells measured as calcium fluxes, versus the untreated condition (Fig. S5).

DISCUSSION

In this work we imaged, for the first time, and showed that, in CEACAM5^{+} CRC cells, the CEACAM5 antigen is concealed at intercellular junctions. In contrast, CD19 and HER2 remain available for interactions with T-cells. With increasing seeding time, we observed non-sustained triggering of CAR T-cells on CRC cell monolayers along with decreased killing of CRC cells by primary T cell-derived CARs. We also observed that the glycocalyx of CRC cells' is ~ 4 and ~ 10 times thicker than that of CAR T-cells and the SLB2, respectively. This could be responsible for the delayed triggering of CAR T-cells at the cell/cell interface versus the SLB2 (Fig. S5). Local treatment with trypsin to disrupt the CRC cell monolayer using a micropipette increased CEACAM5 availability and decreased glycocalyx thickness and as a result, produced faster and sustained calcium fluxes in CAR T-cells and increased killing of CRC cells. Recent studies have shown the increased glycocalyx thickness of cancer cells and that disrupting N-glycosylation boosts CAR T-cell efficacy against solid tumours (*19, 24*). Our results are in good accord with these studies and suggest a crucial role for the glycocalyx in T-cell/tumour interactions. Overall, our study has revealed the mechanism of CEACAM5 CAR T-cell/CRC interactions by establishing combined effects of CEACAM5 availability and glycocalyx thickness, and suggests a possible route for improved therapy. However, this is a model system and studies need to be performed in vivo to determine whether local tissue dissociation is also effective in that setting. A key challenge will be to restrict the effects to the tumour and to avoid disrupting the functions of infiltrating T-cells. In future, we will explore the glycocalyx of other cancer cells and how it affects T-cell triggering.

We found that CD45 exclusion is a potential mechanism of CAR T-cell activation at the CEACAM5 CAR T-cell/CRC cell interface. Along with other studies, our work extends the applicability of the kinetic segregation (KS) model, wherein CD45 exclusion initiates receptor triggering, to CAR T-cells at T-cell/tumour interfaces irrespective of the tumour types (liquid and solid cancer) (*13, 14*).

Recent clinical trial results show the need for a fundamental understanding of CAR T cell triggering (*15*). Our study suggests that CEACAM5 may become increasingly unavailable with CRC progression, thus there might be no accessible CEACAM5 in mCRC tumours. On the contrary, CEACAM5 is more available in normal lung epithelial cells (*15*). Thus, our study offers a ready explanation for the off-target respiratory toxicity of CEACAM5^{+} CAR T-cell/lung epithelial cell interactions. Wu et al. developed an innovative method to direct heat inducible CAR T-cells at the tumour site by local treatment of focused ultrasound (*25*). This could be a potential method to eliminate off-target toxicity for mCRC patients. However, CAR T-cells would still not be able to trigger at the tumour site due to CEACAM5 unavailability and local trypsin treatment may help in this situation.

MATERIALS AND METHODS

Study design

The primary objectives of the study were to: (i) monitor early events of CAR T-cell/CRC cell interaction (ii) identify the barriers to effective treatment (iii) uncover possible routes to tackle these barriers. Using different imaging methods, flow cytometry, imaris and custom-designed analysis pipelines, we found two barriers, CEACAM5 unavailability and thick glycocalyx of CRC cells, of CAR T-cell/CRC interaction. Trypsin delivery using a micropipette improved CAR T-cell/CRC interaction. Random FOVs were chosen for experiments. Experimental replicate number is listed in figure legends.

Isolation and culture of human primary CD8$^+$ T-cells

Fresh peripheral blood was obtained from three healthy donors after informed consent. Peripheral blood mononuclear cells (PBMCs) were enriched by density gradient centrifugation using Ficoll-Paque Plus (GE Healthcare). Naïve CD8 T-cells were isolated from PBMCs using the MagniSort Human CD8 Naïve T-cell enrichment kit according to the manufacturer's instructions (Invitrogen). 1 million naïve CD8$^+$ T-cells were activated with plate-bound anti-CD3 (Biolegend Ultra-LEAF purified, Clone-OKT3, at 1 μg/mL) and anti-CD28 (Biolegend Ultra-LEAF purified, Clone-CD28.2, at 1 μg/mL) for 3 days. Primary CD8$^+$ T-cells were cultured in Immunocult (Stem Cell Technologies) medium supplemented with 50 μg/mL of Gentamicin (Gibco) and 50 U/mL of human recombinant IL-2 (Peprotech). IL-2 was replenished after every 3 days.

Generation of CAR T-cells and overexpression of human CD19 by Sleeping Beauty (SB)

Sleeping beauty (SB) transgene cassettes were used to facilitate overexpression of human CD19 and expression of second-generation CARs targeting human CEACAM5 and CD19. All parental plasmids (pp) were designed and purchased from VectorBuilder. The CD19 SB-CAR was constructed using NEBuilder® HiFi DNA Assembly Master Mix (New England Biolabs, #E2621S) according to the manufacturer’s instructions. The two assembled fragments were PCR-linearized CEACAM-hMN-14 SB-CAR (with the scFv removed) and PCR-amplified anti-CD19 FMC63 single chain variable fragment (scFv) in the VL-Whitlow/218 linker-VH orientation. For CD19 overexpression in LS-174T, a puromycin resistance gene was incorporated into the transposon cassette. For anti-CEACAM5 CAR expression in primary CD8 T-cells, the hMN-14 SB vector was synthesized into a pre-clinical grade (pGC) Gencircle (Genscript Biotech). Stable expression in cell lines was facilitated by SB100X (VectorBuilder), while SB100X mRNA (N1-Methylpseudouridine/m1Ψ) (Genscript Biotech) was employed for

primary $CD8^+$ T-cells. All plasmid transgene cassettes except for SB100X, which uses the CAG promoter, were under control of EF1a.

CAR T Structure

The anti-CEACAM5 scFv comprised variable domains (VH and VL) derived from the clone hMN-14 with FMC63 being used for CD19. In contrast, to anti-CD19 the CEACAM5 variable domains were linked by a poly-Glycine-Serine (G4S)3 linker. Both CAR constructs incorporated a Strep-tag II (WSHPQFEK) sequence and a G4S2 linker, fused between the CD8α hinge and scFv domains to facilitate identification of CAR^+ cells. The transmembrane domain from CD28 was used in conjunction with the intracellular signaling domains of CD28 and CD3ζ.

Nucleofection and selection of SB delivered cassettes

All electroporations were carried out using a Lonza 4D Nucleofector. Briefly, 1-2 million cells were resuspended in their corresponding nucleofection buffer and pulsed according to their respective code (see the following table). Following nucleofection, cells were immediately rescued with 80 µL of pre-warmed complete media (antibiotic-free) and incubated at 37°C for 20 minutes. Subsequently, cells were further diluted and cultured in complete media. LS-174T cells were selected for CD19 expression by the addition of puromycin (1 µg/mL) (Santa-Cruz) for one week. Jurkat CAR^+ cells (anti-CD19 & CEACAM5) were stained with anti-strep-tag II antibody (FITC) and enriched using the EasySep FITC Positive Selection Kit II according to the manufacturer's instructions (StemCell Technologies) (Fig. S1). Conversely, 72-hours post-nucleofection $CD8^+$ CAR T-cells were expanded with plate-bound CEACAM5 protein with FC tag (ACROBiosystems) at 0.5 µg/mL for 4 days in complete Immunocult media with 50 U/mL of human IL-2. The percentage of $CD8^+$ CAR^+ cells was subsequently determined by flow cytometry (Fig. S2).

Cell Type/Line	No. of Cells	Buffer Solution	Pulse Code
Jurkat	1 million	SE	CL-120
LS-174T	1 million	SE	EN-113
Human $CD8^+$ T-cells	2 million	P3	EO-115

Flow Cytometry

Flow cytometry was performed on a CytoFLEX LX Flow Cytometer, with all analysis done on FlowJo software (v10.10). Primary and CRC cell lines were stained for viability with LIVE/DEAD Fixable Near-IR and blocked with Human TruStain FcX (Biolegend) prior to antibody staining. For antibody staining, cells were resuspended in FACS buffer (PBS with 3% FBS). The following antibodies were used: anti-human CD8 Pacific Blue, (Biolegend, RPA-T4), The NWSHPQFEK Tag Antibody FITC, (Genscript, 5A9F9), anti-human CD19 AF594 (Biolegend, HIB19) anti-human CD340/HER-2 AF647 (Biolegend, 24D2) and anti-human CEACAM5/CD66e PE (R&D Systems, 487609). Cells were fixed in IC Fixation Buffer (eBioscience) and washed in FACS buffer twice prior to acquisition.

Jurkat CAR T-cell and CRC cell culture

Jurkat CAR T-cells ($CEACAM5^+$, $CD19^+$) and CRC cells ($CEACAM5^+$ & $HER2^+$ WT LS-174T, $CEACAM5^-$ RKO, $CD19^+$ LS-174T) were cultured in StableCell™ RPMI-1640 and DMEM/F-12 (1:1) (1X) + GlutaMAX™-I (Dulbecco's Modifies Eagle Medium F-12 Nutrient Mixture (Ham)) medium, respectively. Both medium was supplemented with 10 % (v/v) fetal calf serum (FCS), 1 % (v/v) HEPES buffer solution (1M), 1 % (v/v) sodium pyruvate 100 mM (100X) and 1 % (v/v) pen strep antibiotics. Hereafter, we will call the supplemented media as 'complete RPMI' and 'complete DMEM'. TrypLE™ express enzyme was used to detach the CRC cells. Cells were then diluted and re-suspended in complete DMEM for further culture.

CRC cells were passaged before they could grow confluent. All cell culture was performed in HEPA-filtered cell culture cabinets and cells were grown within the incubator with 37^0C and 5 % CO_2 maintaining density 0.2-0.5 million/ml.

SLB2 preparation and monitoring CAR T-cell/SLB2 interaction using imaging

A mixture of 98:2 mol% POPC (Avanti Polar Lipids) and DGS-NTA-Ni^{2+} (NiNTA; Avanti Polar Lipids) was prepared as previously described for making SLB2 using the vesicle fusion technique (*16*). SLB2 protein mixture presents CD58 and ICAM-1, CD45 and CD43, human CEACAM5/CD66e protein (from ACROBiosystems), and gp100-MHC. CD45 and CD43 proteins have been conjugated covalently with Alexa-555 using random lysine before use. CEACAM5 targeting Jurkat CAR T-cells were labelled with a mixture of Fluo-4-AM (calcium indicator) and Cell-Mask Deep Red Plasma Membrane Stain (ThermoFisher) before being allowed to interact with SLB2. As experimental readouts, calcium signaling, cell footprint, and close-contact (CD45/CD43 exclusion) formation were measured using a home-built microscope. Individual protein concentrations of CEACAM5$^+$ and CEACAM5$^-$ SLB2s are given below:

	CEACAM5$^+$SLB2	CEACAM5$^-$SLB2
Protein	Conc. (ng/µL)	
CEACAM5	0.5	0
gp100-MHC	9.5	10
CD58	0.5	0.5
ICAM-1	1.2	1.2
CD45	2.5	2.5
CD43	1.5	1.5

Details of protein production, labelling, SLB2 preparation and experiments have been described in our previous publication (*16*).

TIRF Microscopy

The interaction of CAR T-cell/SLB2 was imaged using a home-built microscope in total internal reflection fluorescence (TIRF) mode with three laser lines: 488 nm (200 mW, iBeam-SMART, Toptica), 561 nm (LPX-561L, LaserBoxx, Oxxius), and 641 nm (Obis, Coherent). Each laser line was attenuated by neutral density filters, expanded by a pair of plano-convex lenses, circularly polarised by a quarter-wave plate, and combined in the downstream path by appropriate dichroic mirrors. The lasers were then aligned and directed to the edge of a 100X oil-immersion objective lens (CFI Apo TIRF 100XC Oil, NA 1.49, MRD01991, Nikon), which was mounted on an inverted optical microscope (Eclipse Ti2, Nikon). Fluorescence emission was collected through the same objective lens, and a quad-band dichroic mirror (Di01-R405/488/561/635, Semrock) was used to separate the emission from the excitation light. The built-in 1.5X magnifying lens in the Ti2 microscope body was used to further improve the image resolution. Emission was then filtered through appropriate long-pass and single-band filters (BLP01-488R + FF01-520/44-25, LP02-568RS-25 + FF01-587/35-25, FF01-692/40-25; Semrock) before being collected by an EMCCD camera (Evolve 512 Delta, Photometrics). The microscope was equipped within an incubator (DigitalPixel) to maintain 37 °C during live T-cell imaging. The built-in Perfect Focus System (PFS) of the TI2 microscope body was used to maintain focus during imaging, and three-colour images were acquired sequentially using Micro-Manager 2.0.0 software with a 100 ms exposure time and a 2-second interval. The pixel size of the collected images was 107 nm, measured using a line grating target (R1L3S6P, Thorlabs).

CAR T-cell/SLB2 imaging data analysis

Data was analysed using a custom-written code described in our previous publication (*16*).

CRC cells' (WT LS-174T, LS-1034, RKO, CD19^{+} LS-174T) monolayer preparation

The viability of the adherent CRC cells was checked and counted using Countess II automated cell counter (ThermoFisher) by mixing with 1:1 trypan blue (0.4%). The cells were plated on ibidi glass bottom (35 mm, high) dish / 8 well plate maintaining 0.3-0.6 million/ml and incubated for seeding for 24 and 48 hrs (early and longer, respectively).

Calcium imaging and analysis

On the day of the experiment, CAR T-cells were labelled with Fluo-4-AM and allowed to interact with CRC cells' monolayer. As previously mentioned, a 488 nm laser was used for excitation, and epifluorescence calcium imaging of CAR T-cells was monitored at the T-cell/tumour interface. Imaging was performed with an exposure time of 100 ms with a 30-second interval. Initially, a 20X objective lens (Plan Fluor, NA 0.50, Nikon) was used to capture a large field of view (FOV) of T-cell/tumour interactions. Subsequently, a 60X oil-immersion objective lens (CFI Apo TIRF 60XC Oil, NA 1.49 oil-immersion, MRD01691, Nikon) was used for close inspection. The pixel size of the collected images using 20X and 60X objective lens were 800 nm and 178 nm, respectively.

Calcium imaging time-stacks were analysed using the TrackMate plugin in ImageJ/Fiji (*26*). Cells within the imaging FOVs were detected and segmented using the StarDist (*27*) detector in TrackMate with default parameters. These segmented cells were linked into trajectories using the simple LAP tracker to capture the dynamics of a T-cell in all frames throughout the movie. Parameters for linking max distance, gap-close max distance and gap-close max frame gap were set to ensure that segmented cells from the same cell across different frames were accurately joined. Typical parameters were 15 μm for max distances and 10 frames for max frame gap. TrackMate outputted a list of polygon regions of interest (ROI) for the segmented

cells, with each ROI labelled according to the track it belonged to. The mean fluorescence intensity of each cell across all frames was measured using the Measure function in ImageJ/Fiji (Fig. S16). The results and the ROI information were saved to local files and organized using a home-written Python script, which processed the data to output intensity information as a function of time for each individual cell. Mean fluorescence intensity (I_0 indicates the first frame where T cell activity is detected; I_t denotes the subsequent frames over time) was extracted and the ratio (I_t/I_0) was plotted as a function of time for each cell using OriginPro 2023b. Calcium imaging data was further analyzed using OriginPro 2023b to determine the residuals and envelope (Fig. S6-S8).

CAR accumulation experiment

FITC conjugated anti-strep-tag II antibody was used to label the strep-tag II of the CEACAM5$^+$ Jurkat CAR T-cells and they were allowed to interact with early seeded LS-174T monolayer. A 488 nm laser with 100 ms exposure time was used as excitation source and CAR accumulation was monitored by epifluorescence imaging with time (Movie S4).

Glycocalyx measurement of T-cell and LS-174T using super-resolution imaging

CAR T-cells and early, longer seeded LS-174T cells were fixed using a mixture of 0.8 % paraformaldehyde (28906, Thermo Scientific, MA) and 0.2 % glutaraldehyde (G5882, Sigma-Aldrich) at room temperature. Fixed CAR T-cells were allowed to settle on the poly-L-lysine (PLL, 150-300 kDa; P4832; Sigma-Aldrich) coated coverslip for 45 min as described in our earlier publication (*21*). Sodium carbonate-bicarbonate buffer with pH 9.6 was used to dilute HMSiR conjugated wheat germ agglutin (WGA) and used to label the glycocalyx of the cells. A 641 nm laser in highly inclined and laminated optical sheet (HILO) mode was used to excite the sample and 20000 frames were collected with 30 ms exposure time. 2D resPAINT super-

resolution imaging data was analysed in Fiji using PeakFit (GDSC SMLM 2.0) and shown in Fig. 2 (*21*).

Diluted 0.05% Trypsin-EDTA (1X, gibco) was used for bulk treatment of early and longer seeded LS-174T monolayers. Trypsin treated monolayers were washed and fixed as described before. resPAINT imaging was carried out and the results are shown in Fig. 4F.

Antigen mapping on LS-174T monolayer using antibody

PE conjugated anti-hCEACAM5 (mouse IgG_{2A}, R & D Systems), Alexa Fluor 594 conjugated anti-hCD19 (mouse IgG_1, R & D Systems) and Alexa Fluor 647 conjugated anti-human CD340 (erbB2/HER-2, Biolegend) antibodies were used for CEACAM5, CD19 and HER2 mapping, respectively. Respective lasers were used for excitation to monitor epifluorescence imaging.

Granules release experiment and analysis using Imaris

Primary CAR T-cells were labelled with a mixture of Fluo-4-AM and lysotracker red (50 nM) and allowed to interact with early seeded LS-174T monolayer. 488 nm and 561 nm lasers were used for excitation and epifluorescence imaging was collected to monitor calcium flux and granule release by CAR T-cells simultaneously (Fig. 3B-D).

Granules release analysis using Imaris

Released granules from individual T-cells were tracked using Imaris 10.0.1 (Oxford Instruments). The surface function with tracking was utilized for detecting the granules. This tool allows us to create an artificial solid object (surfaces) to represent the range of interest of a specific object, like granules here. The automatic surface creation wizard in Imaris was used for segmenting granules, followed by fine-tuning the segmentation for accuracy. We used in-built tools in Imaris for this purpose, which involves adjusting the contour of the surface or correcting any segmentation errors. To make the surfaces more visible, we assigned different

colours and opacity to the created surfaces. We then tracked the resulting surfaces over time using an autoregressive motion tracking algorithm. Several parameters, such as track length, track speed mean, and track straightness, were computed.

Track length: The Track Length (tl) is the total length of displacements within the Track.

Track speed mean: The mean value of the cell's speed on the track. Mean speed is determined by dividing track length by the time between first and last object in the track.

Track straightness:

$$S = \frac{D}{L}$$

S = Track Straightness

D = Track Displacement

L = Track Length

Segmenting and Tracking CAR T-cells using Imaris

Calcium imaging movies of Jurkat CAR T-cell/LS-174T interaction monitored using 60X objective lens was used for analyzing track speed mean and track straightness of CAR T-cells using Imaris as described in previous section.

Imaging CD45 exclusion at T-cell/tumour cell interface using eSPIM

Optical Setup

The experiment employed an open-top single-objective light sheet microscope based on the Oblique Plane Microscopy (OPM) configuration (*28*). The instrument adopted a similar design as reported by Yang et al (*29*). A primary 60X NA 1.27 water-immersion objective (CFI Plan Apo IR 60XC WI, Nikon) mounted on an inverted microscope body (Eclipse Ti-U, Nikon) was used for both light sheet launching and emission collection. Two continuous diode lasers, 488

nm (200 mW, LBX-488-200, Oxxius) and 638 nm (180 mW, 06-MLD-638, Cobolt), were expanded, collimated and combined into a single excitation path. The combined beam then passed through a cylindrical lens to generate a 1D Gaussian beam. A quad-band dichroic mirror (Di01-R406/488/561/635, Semrock) was used to separate the excitation and emission wavelengths. The beam propagated through two 4f systems before entering the primary objective at one edge of the back focal plane (BFP) to produce a 30-degree-tilted light sheet. Rapid volumetric illumination was achieved by scanning the light sheet using a 1-D Galvo mirror (GVS201, Thorlabs). The operation of the galvo mirror was controlled by a home-written LabView script.

Fluorescence collected by the primary objective was transmitted through the quad-band dichroic mirror, relayed onto a 40X secondary air objective (CFI Plan Apo Lambda D Air, NA 0.95, Nikon), with the pupil plane conjugated to that of the primary objective. Subsequently, the emission was collected by a bespoke glass-tipped tertiary objective (AMS-AGY v1.0, NA 1, Calico lab) oriented at a 30-degree angle to the optical axis. A tube lens (F = 321 mm) was used to direct the emission onto a sCMOS camera (Photometrics Prime 95B). Additionally, the setup featured a three-colour optical splitter (OptoSplit III, Prior) for simultaneous multi-colour imaging.

Experimental Details

LS-174T and Jurkat CAR T-cells were labelled with Alexa Fluor 647 anti-human CD326 (Ep-CAM, clone 9C4, BioLegend) antibody and Alexa Fluor 488 anti-CD45 monoclonal antibody (Gap8.3), respectively and CAR T-cells were allowed for interaction with early seeded LS-174T monolayer and incubated for 30 mins to image late-stage contact formation. Volumetric scans were performed using a home-written automation script in μManager 2.0. During each volumetric scan, the light sheets from the 488 nm (44.4 W/cm^2) and 638 nm (55.5 W/cm^2)

lasers scanned through the sample. The detection camera was synchronised with the galvo scanning, enabling simultaneous three-colour imaging with an exposure time of 30 ms. Each volumetric scan consisted of 100 frames (full 1200 x 1200 pixel FOV) acquired within approximately 4 seconds.

To monitor the late-stage dynamics at CAR T-cell/LS-174T cell interface, volumetric scans were repeated every 30 seconds for approximately 40-45 minutes. Throughout the acquisition process, the sample stage and the primary objective were enclosed within a sealed plastic chamber. The temperature around the sample was maintained at 37°C. The acquired images from each volumetric scan were deskewed and reconstructed into 3D projections using a custom Python script.

Micropipette preparation and trypsin delivery

Micropipette fabrication

Micropipettes were fabricated from borosilicate glass capillaries (World Precision Instruments, 1B150F-4), with an outer and inner diameter of 1.5 and 0.84 mm, respectively. A laser pipette puller was used for fabrication (Model P-2000, Sutter Instrument, CA) with the following parameters: (Line 1) Heat = 415, FIL = 4, VEL = 30, DEL = 200. This pulled a micropipette with a pore diameter of approximately 4-5 µm (Fig. S17).

Micropipette delivery

The micropipette was controlled using a 3D manipulator (Scientifica PatchStar Micromanipulator, Scientifica, Uckfield, UK) to provide precise positioning of the tip above the cell. A continuous pressure pulse (0.7 psi or 5 kPa) was used to deliver trypsin, until clear disruption of the cell contacts in the 2nd layer was observed. Careful control of the pressure pulse ensured that the cell monolayer was not disturbed in this process. A similar strategy was employed for local delivery of the fluorescent antibody.

Brightfield imaging

Brightfield and epifluorescence images were collected simultaneously.

Statistical analysis

Statistical analysis was performed using Graphpad Prism 10.3.0. Two-sided paired and unpaired Student's t-test were performed to compare the glycocalyx thickness of early vs. longer seeded LS-174T and CAR T-cell vs. LS-174T cell, respectively.

Supplementary Materials

This PDF file includes:

Fig. S1 to S17

Movie legends for S1 to S17

The following link includes:

Movie S1 to S17

https://drive.google.com/drive/folders/1s0fVKN7kppKKBt71s4GxqXmIe55VoNGc?usp=sharing

REFERENCES AND NOTES

(1) G. Gross, T. Waks, Z. Eshhar, Expression of immunoglobulin-T-cell receptor chimeric molecules as functional receptors with antibody-type specificity. *Proc Natl Acad Sci U S A* **86(24)**, 10024-8 (1989).

(2) C. H. June, R. S. O'Connor, O. U. Kawalekar, S. Ghassemi, M. C. Milone, CAR T cell immunotherapy for human cancer. *Science* **359(6382)**, 1361-1365 (2018).

(3) D. L. Porter, B. L. Levine, M. Kalos, A. Bagg, C. H. June, Chimeric antigen receptor-modified T cells in chronic lymphoid leukemia. *N Engl J Med* **365(8)**, 725-33 (2011).

(4) S. L. Maude, N. Frey, P. A. Shaw, R. Aplenc, D. M. Barrett, N. J. Bunin, A. Chew, V. E. Gonzalez, Z. Zheng, S. F. Lacey, Y. D. Mahnke, J. J. Melenhorst, S. R. Rheingold, A. Shen, D. T. Teachey, B. L. Levine, C. H. June, D. L. Porter, S. A. Grupp, Chimeric antigen receptor T cells for sustained remissions in leukemia. *N Engl J Med* **371(16)**, 1507-17 (2014).

(5) G. Guzman, M. R. Reed, K. Bielamowicz, B. Koss, A. Rodriguez, CAR-T Therapies in Solid Tumors: Opportunities and Challenges. *Curr Oncol Rep.* **25(5)**, 479-489 (2023).

(6) S. M. Albelda, CAR T cell therapy for patients with solid tumours: key lessons to learn and unlearn. *Nat. Rev. Clin. Oncol.* **21**, 47-66 (2024).

(7) X. Qin, F. Wu, C. Chen, Q. Li, Recent advances in CAR-T cells therapy for colorectal cancer. *Front Immunol.* **13**, 904137 (2022).

(8) B. Ghazi, A. E. Ghanmi, S. Kandoussi, A. Ghouzlani, A. Badou, CAR T-cells for colorectal cancer immunotherapy: Ready to go? *Front Immunol.* **13**, 978195 (2022).

(9) J. Weng, S. Li, Z. Zhu, Q. Liu, R. Zhang, Y. Yang, X. Li, Exploring immunotherapy in colorectal cancer. *J Hematol Oncol.* **15**, 95 (2022).

(10) D. C. Harrer, S. -S. Li, M. Kaljanac, M. Barden, H. Pan, H. Abken, Fine-tuning the antigen sensitivity of CAR T cells: emerging strategies and current challenges. *Front. Immunol.* **14,** 01-09 (2023).

(11) L. Wu, J. Brzostek, P. D. S. Vale, Q. Wei, C. K.T. Koh, J. X. H. Ong, L. -z. Wu, J. C. Tan, Y. L. Chua, J. Yap, Y. Song, V. J. Y. Tan, T. Y. Y. Tan, J. Lai, P. A. MacAry, N. R.J. Gascoigne, CD28-CAR-T cell activation through FYN kinase signaling rather than LCK enhances therapeutic performance. *Cell Rep. Med.* **4,** 100917 (2023).

(12) A. J. Davenport, R. S. Cross, K. A. Watson, Y. Liao, W. Shi, H. M. Prince, P. A. Beavis, J. A. Trapani, M. H. Kershaw, D. S. Ritchie, P. K. Darcy, P. J. Neeson, M. R. Jenkins, Chimeric antigen receptor T cells form nonclassical and potent immune synapses driving rapid cytotoxicity. *Proc Natl Acad Sci U S A* **115(9)**, E2068-E2076 (2018).

(13) Q. Xiao, X. Zhang, L. Tu, J. Cao, C. S. Hinrichs, X. Su, Size-dependent activation of CAR-T cells. *Sci. Immunol.* **7**, eabl3995 (2022).

(14) S. J. Davis, P. A. van der Merwe, The kinetic-segregation model: TCR triggering and beyond. *Nat. Immunol.* **7**, 803-809 (2006).

(15) F. C. Thistlethwaite, D. E. Gilham, R. D. Guest, D. G. Rothwell, M. Pillai, D. J. Burt, A. J. Byatte, N. Kirillova, J. W. Valle, S. K. Sharma, K. A. Chester, N. B. Westwood, S. E. R. Halford, S. Nabarro, S. Wan, E. Austin, R. E. Hawkins. The clinical efficacy of first-generation carcinoembryonic antigen (CEACAM5)-specific CAR T cells is limited by poor persistence and transient pre-conditioning-dependent respiratory toxicity. *Cancer Immunol Immunother.* **66(11)**, 1425-1436 (2017).

(16) E. Jenkins, M. Körbel, C. O'Brien-Ball, J. McColl, K. Y. Chen, M. Kotowski, J. Humphrey, A. H. Lippert, H. Brouwer, A. M. Santos, S. F. Lee, S. J. Davis, D. Klenerman,

Antigen discrimination by T cells relies on size-constrained microvillar contact. *Nat. Commun.* **14**, 1611 (2023).

(17) R. A. Morgan, J. C. Yang, M. Kitano, M. E. Dudley, C. M. Laurencot, S. A. Rosenberg, Case report of a serious adverse event following the administration of T cells transduced with a chimeric antigen receptor recognizing ERBB2. *Mol Ther.* **18(4)**, 843-51 (2010).

(18) L. Möckl, The Emerging Role of the Mammalian Glycocalyx in Functional Membrane Organization and Immune System Regulation. *Front. Cell. Dev. Biol.* **8**, 253 (2020).

(19) L. Möckl, K. Pedram, A. R. Roy, V. Krishnan, A.-K. Gustavsson, O. Dorigo, C. R. Bertozzi, W. E. Moerner, Quantitative Super-Resolution Microscopy of the Mammalian Glycocalyx. *Dev. Cell* **50**, 57-72 (2019).

(20) S. Park, M. J. Colville, J. H. Paek, C. R. Shurer, A. Singh, E. J. Secor, C. J. Sailer, L.-T. Huang, J. C. -H. Kuo, M. C. Goudge, J. Su, M. Kim, M. P. DeLisa, S. Neelamegham, J. Lammerding, W. R. Zipfel, C. Fischbach, H. L. Reesink, M. J. Paszek, Immunoengineering can overcome the glycocalyx armour of cancer cells. *Nat. Mater.* **23,** 429-438 (2024).

(21) E. W. Sanders, A. R. Carr, E. Bruggeman, M. Körbel, S. I. Benaissa, R. F. Donat, A. M. Santos, J. McColl, K. O'Holleran, D. Klenerman, S. J. Davis, S. F. Lee, A. Ponjavic, resPAINT: Accelerating Volumetric Super-Resolution Localisation Microscopy by Active Control of Probe Emission. *Angew. Chem.Int. Ed.* **61**, e2022069 (2022).

(22) S. Benchimol, A. Fuks, S. Jothy, N. Beauchemin, K. Shirota, C. P. Stanners, Carcinoembtyonic Antigen, a Human Tumor Marker, Functions as an Intercellular Adhesion Molecule. *Cell* **57**, 327-334 (1989).

(23) S. M. Cox, P. S. Baur, B. Haenelt, Retention of the glycocalyx after cell detachment by EGTA. *J Histochem Cytochem.* **25(12)**, 1368-72 (1977).

(24) B. Greco, V. Malacarne, F. D. Girardi, G. M. Scotti, F. Manfredi, E. Angelino, C. Sirini, B. Camisa, L. Falcone, M. A. Moresco, K. Paolella, M. D. Bono, R. Norata, F. Sanvito, S. Arcangeli, C. Doglioni, F. Ciceri, C. Bonini, A. Graziani, A. Bondanza, M. Casucci, Disrupting N-glycan expression on tumor cells boosts chimeric antigen receptor T cell efficacy against solid malignancies. *Sci. Transl. Med.* **14**, eabg3072 (2022).

(25) Y. Wu, Y. Liu, Z. Huang, X. Wang, Z. Jin, J. Li, P. Limsakul , L. Zhu, M. Allen, Y. Pan, R. Bussell, A. Jacobson, T. Liu, S. Chien, Y. Wang, Control of the activity of CAR-T cells within tumours via focused ultrasound. *Nat BioMed Eng.* **5(11)**, 1336-47 (2021).

(26) D. Ershov, M.-S. Phan, J. W. Pylvänäinen, S. U. Rigaud, L. L. Blanc, A. C. -Orszag, J. R. W. Conway, R. F. Laine, N. H. Roy, D. Bonazzi, G. Duménil, G. Jacquemet, J. -Y. Tinevez, TrackMate 7: integrating state-of-the-art segmentation algorithms into tracking pipelines. *Nat. Methods* **19**, 829-832 (2022).

(27) U. Schmidt, M. Weigert, C. Broaddus, G. Myers, Cell detection with star-convex polygons, *Medical Image Computing and Computer Assisted Intervention - Miccai 2018*, **Part II**, 265-273 (2018).

(28) C. Dunsby, Optically sectioned imaging by oblique plane microscopy. *Opt Express.* **16(25)**, 20306-16 (2008).

(29) B. Yang, X. Chen, Y. Wang, S. Feng, V. Pessino, N. Stuurman, N. H. Cho, K. W. Cheng, S. J. Lord, L. Xu, D. Xie, R. D. Mullins, M. D. Leonetti, B. Huang, Epi-illumination SPIM for volumetric imaging with high spatial-temporal resolution. *Nat. Methods.* **16(6)**, 501-504 (2019).

Acknowledgments: We gratefully acknowledge the flow cytometry facility from the School of the Biological Sciences for their support and assistance, and Cambridge Advanced Imaging Centre (CAIC) for providing access to their data analysis workstation and softwares. Additionally, we would also like to give thanks to Genscript Biotech for kindly providing pre-clinical grade Gencircles and SB100X mRNA (N1-Methylpseudouridine/m1Ψ).

Funding: This work was supported by Horizon Europe Marie Skłodowska-Curie Actions (MSCA) guarantee grant award (Project no. MBAG/773, Award no. G114341) provided by the UK Research and Innovation (UKRI), and Cancer Research UK (CRUK) grant (award reference DRCCIPA\100010). B.M. is supported by CRUK Career Development Fellowship (RCCFEL\100095), NSF-BIO/UKRI-BBSRC project grant (BB/V006126/1), and MRC project grant (MR/V028995/1).

Author contributions: Conceptualization: D.B. and D.K. Methodology: D.B., P.S., B.L., D.H., S.K., Z.Z., S.J.D., and D.K. Cells and reagents provided: C.W., J.P.R., M.A.C., S.J.D., and B.M. Investigation: D.B., C.W., P.S., B.L., and D.H. Visualization: D.B., C.W., S.K., and Z.Z. Funding acquisition: D.B., B.M., S.J.D., and D.K. Project administration: D.B. and D.K. Supervision: D.K. Writing-original draft: D.B. and D.K. Writing-review & editing: D.B., S.J.D., B.M., D.K.

Competing interests:

The authors declare that they have no competing interests.

Data and materials availability:

All imaging data needed to evaluate the conclusions in the paper are present in the paper and the supplementary materials and movies. Tabulated underlying data from individual figures are provided in data file S1. Codes are available in Github

(https://github.com/mkoerbel/contactanalysis_2D & https://github.com/Zui409). All additional datasets of the current study are available from the corresponding authors on request.

Figures:

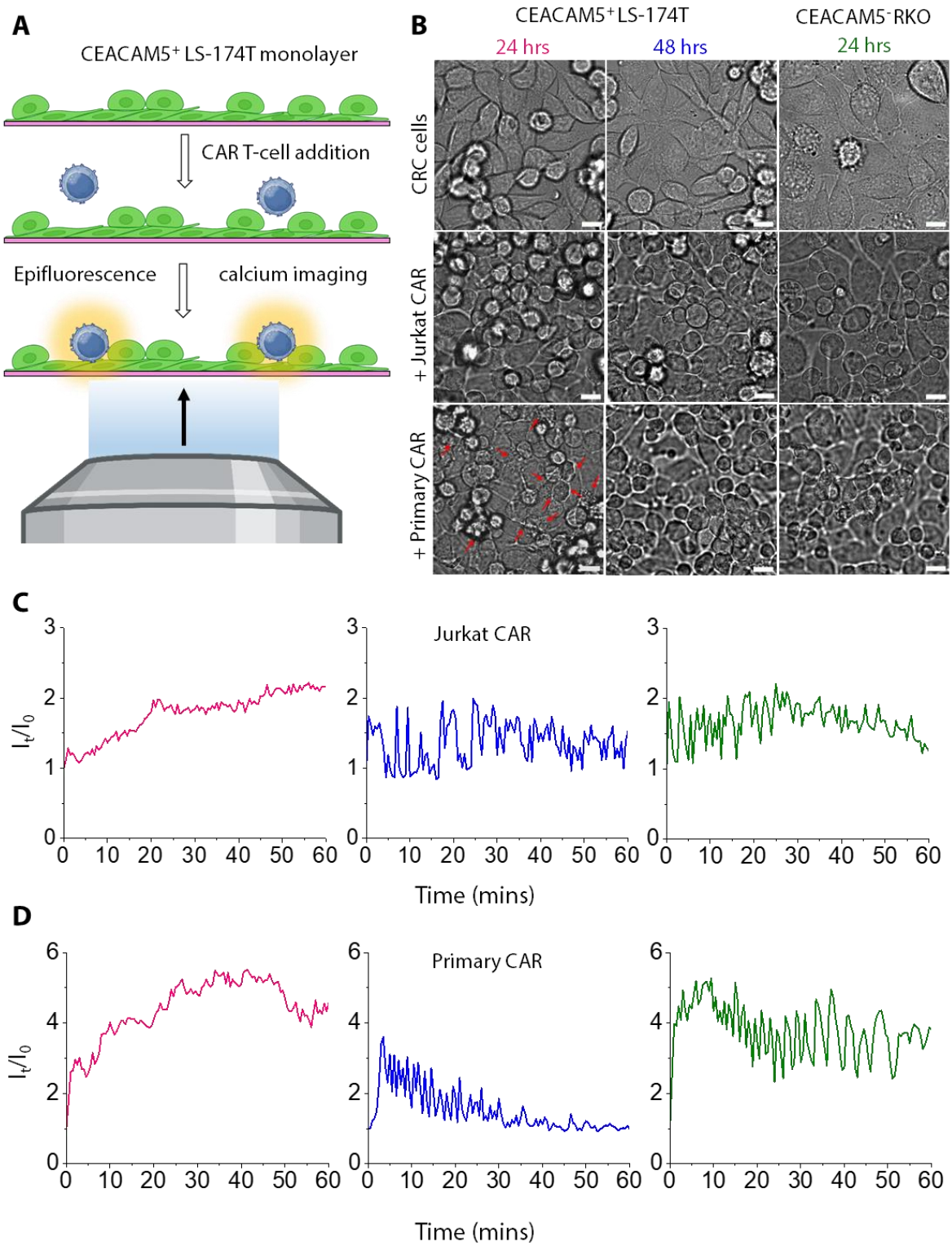

Fig. 1. CAR T-cell/CRC cell interaction. (A) Cartoon shows CAR T-cells interacting with CEACAM5$^+$ LS-174T cell monolayer. Live T-cell/tumour interaction was monitored using

epifluorescence calcium and brightfield imaging. (B) Brightfield images show differently seeded LS-174T (pink, blue: 24 and 48 hrs, respectively) and CEACAM5^{-} RKO monolayers (olive: 24 hrs) interacting with Jurkat and primary CAR T-cells. Red arrows indicate killing of LS-174T cells by primary CAR T-cells. Scale bars are 10 μm. The same colour code will be used hereafter throughout all figures. (C & D) Representative epifluorescence calcium flux colour coded traces of Jurkat and primary CAR T-cells while interacting with LS-174T and RKO monolayers. For each seeding condition, results are representative of 6-7 (n = 6-7) and 3-4 (n = 3-4) FOVs for Jurkat CAR T-cell/CRC and primary CAR T-cell/CRC interactions, respectively.

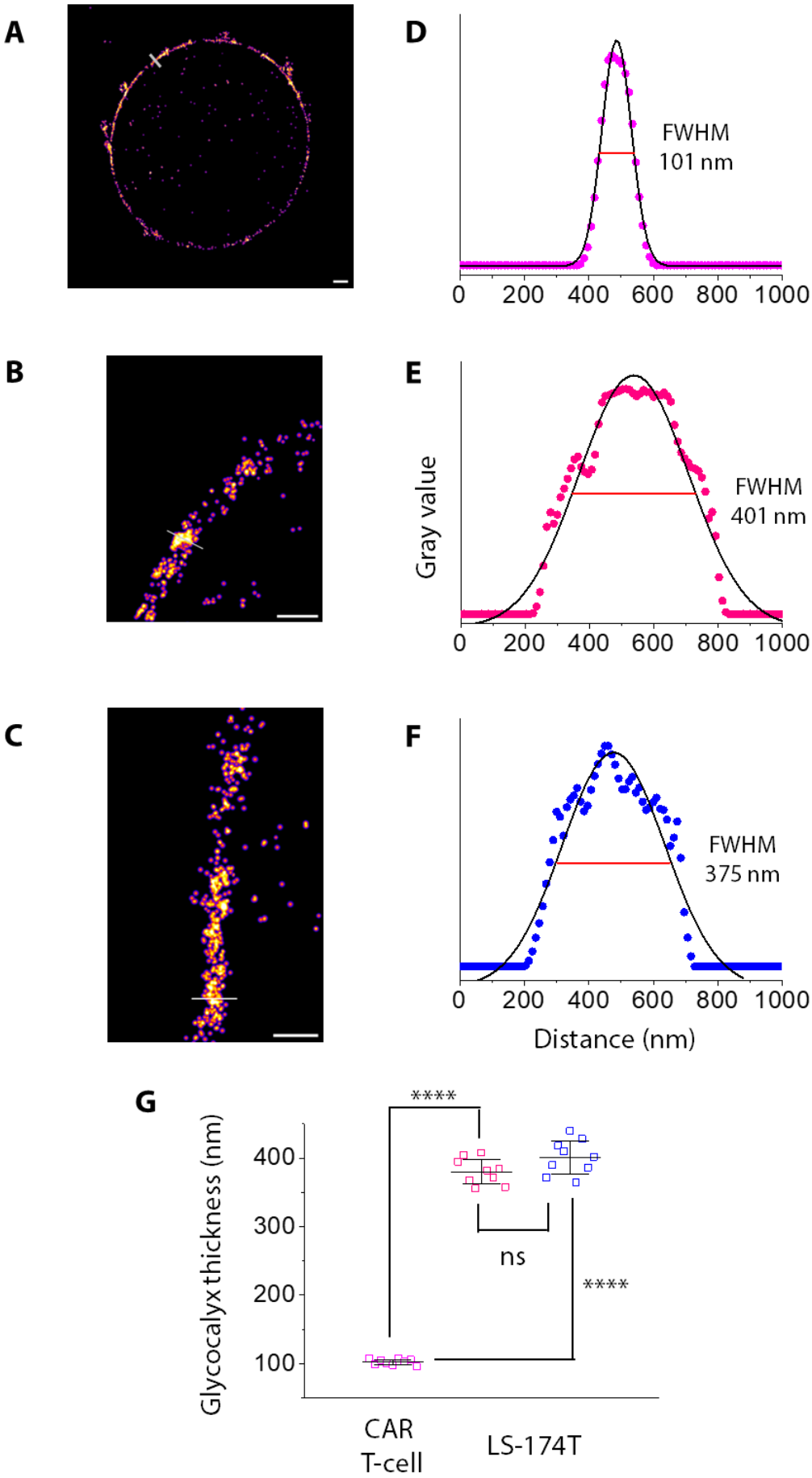
A
D
FWHM
101 nm
0
200
400
600
800
1000
B
E
Gray value
FWHM
401 nm
0
200
400
600
800
1000
C
F
FWHM
375 nm
0
200
400
600
800
1000
Distance (nm)
G
Glycocalyx thickness (nm)
400
300
200
100
****
ns
****
CAR
T-cell
LS-174T

Fig. 2. Super-resolution (resPAINT) (*21*) imaging of the glycocalyx. Representative 2D images of (A) CAR T-cell and (B-C) LS-174T cell (24 and 48 hrs seeded, respectively) glycocalyces labelled with WGA-HMSiR. Scale bars are 1 µm. (D-F) Colour coded line profiles from panels A-C. Glycocalyx thickness was determined as the FWHM of the Gaussian fit. (G) Variation in glycocalyx thickness shows ~ 4 times thicker glycocalyx of LS-174T cell than CAR T-cell. For each condition, data points were extracted by measuring thickness at multiple locations of three individual images (n = 3) collected from three independent experiments. Error bars depict (mean ± standard deviation). P values were determined using Student's t-test. ****$P < 0.0001$, ns not significant.

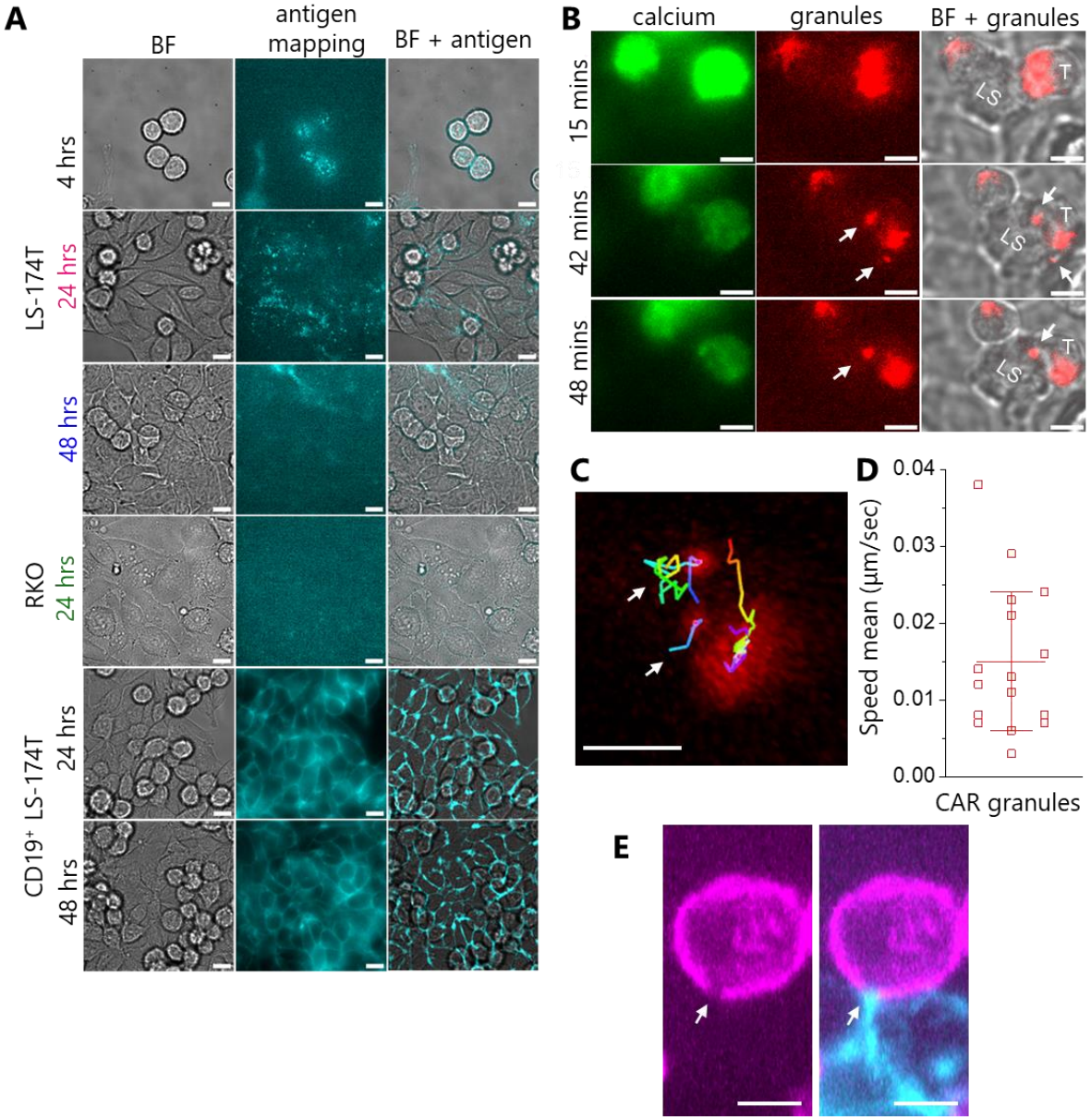

Fig. 3. Antigen mapping, granules recruitment and CD45 exclusion. (A) Middle column shows CEACAM5 and CD19 mapping on LS-174T, RKO and CD19^{+} LS-174T cells, respectively at different seeded conditions described on the left. The left and right columns show brightfield (BF) and merged (brightfield and antigen mapping) images, respectively. For each seeding condition, images are representative of 10-15 (n = 10-15) FOVs. (B) Time series of calcium flux (left column), granules recruitment (white arrows in middle and right columns) and merged (white light and granules) images show the sequence of events during primary CAR T-cell/LS174T (24 hrs seeded) interaction. Results are representative of 8-9 events (n = 8-9)

collected from 3 individual FOVs. (C-D) Tracks (white arrows in ‘C’) and track speed mean of granules were determined using Imaris 10.0.1. Error bar depicts (mean ± standard deviation). (E) CD45 exclusion (white arrow) at Jurkat CAR T-cell (magenta)/LS-174T (cyan) cell interface was captured using epifluorescence selective plane illumination microscopy (eSPIM). We studied 12-16 (n = 12-16) FOVs. Scale bars are 10 μm and 5 μm in A-C and E, respectively.

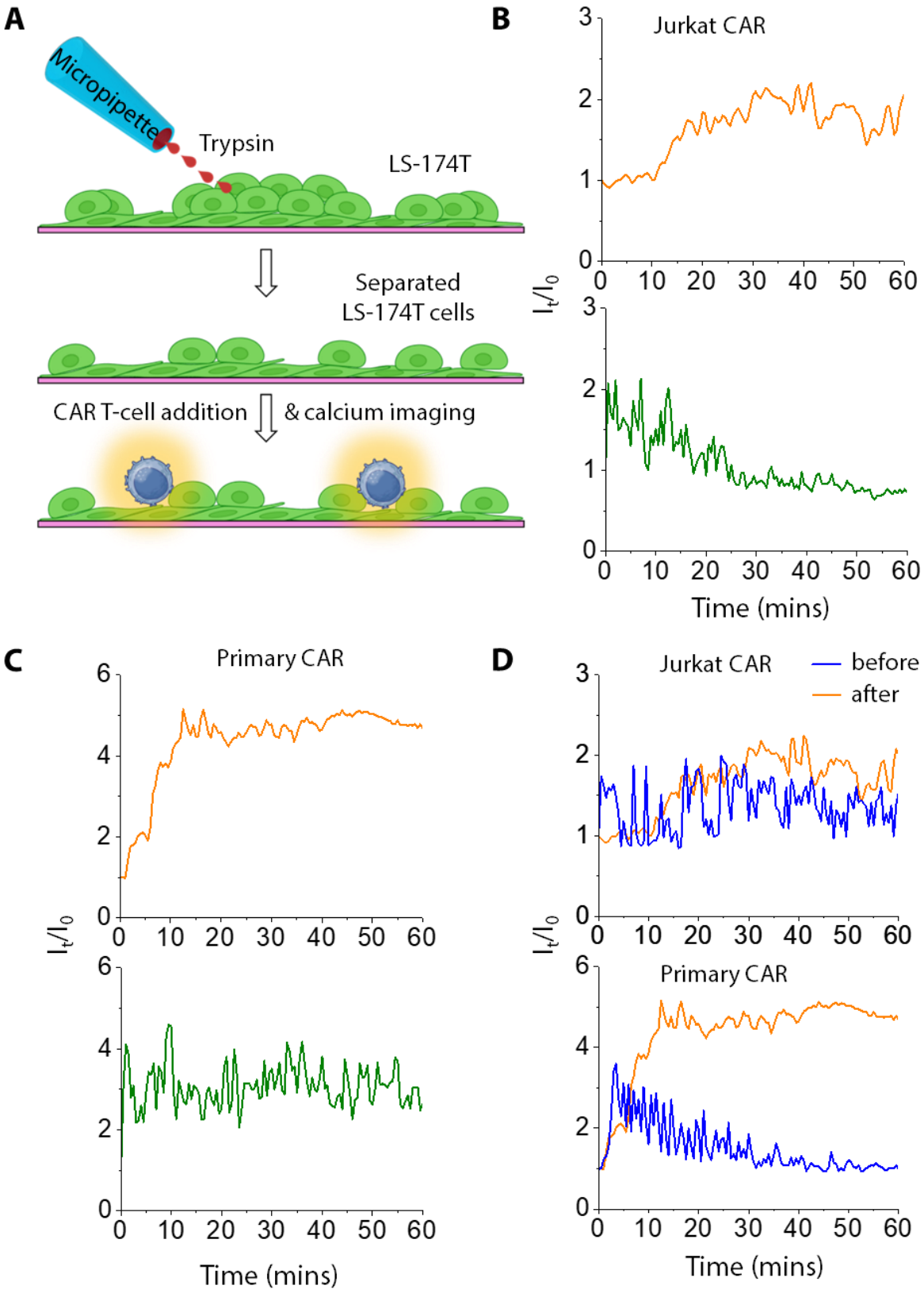
A
Micropipette
Trypsin
LS-174T
Separated
LS-174T cells
CAR T-cell addition
& calcium imaging
B
Jurkat CAR
I_t/I_0
Time (mins)
C
Primary CAR
I_t/I_0
Time (mins)
D
Jurkat CAR
before
after
I_t/I_0
Primary CAR
Time (mins)

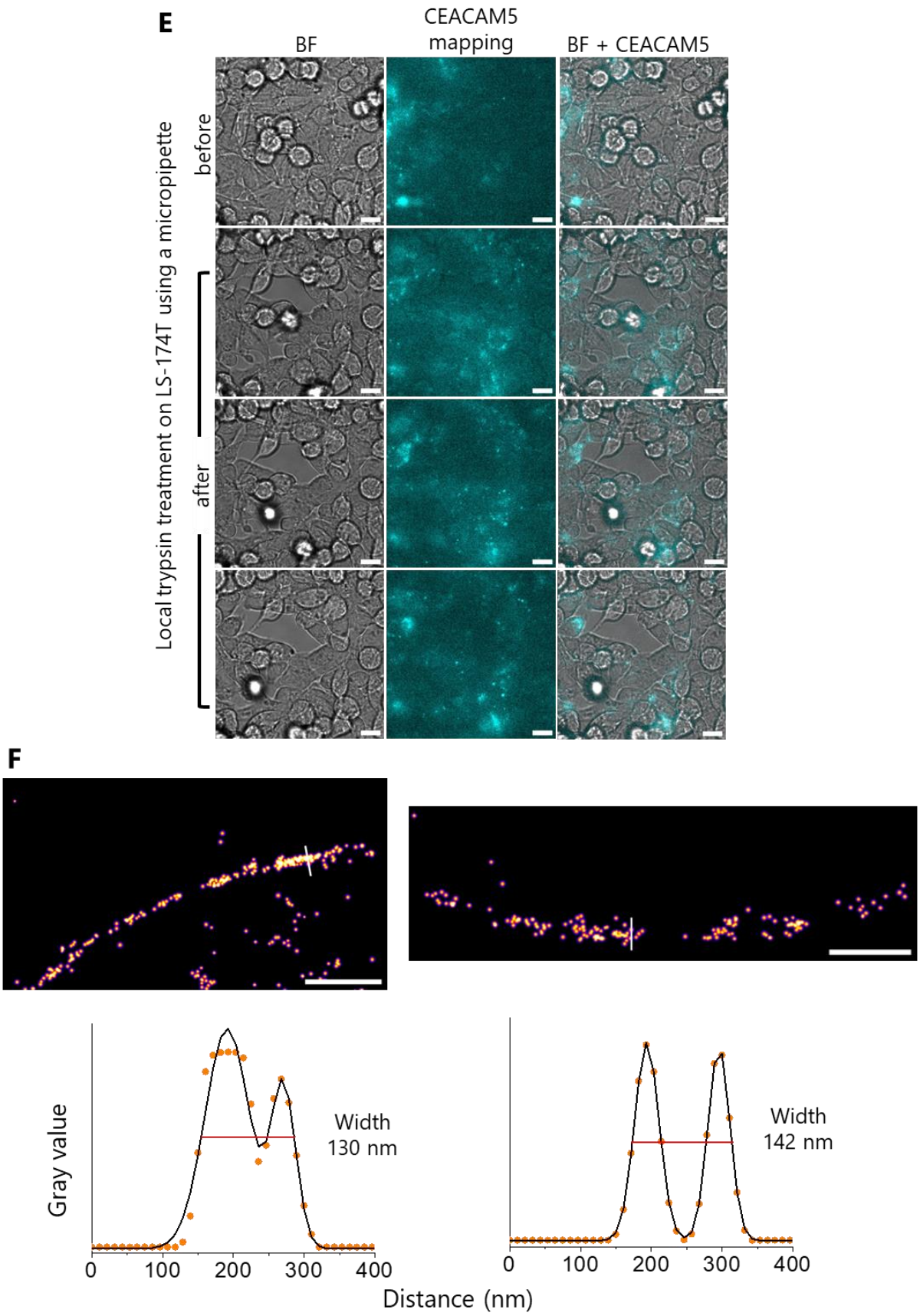
E
BF
CEACAM5 mapping
BF + CEACAM5
before
after
Local trypsin treatment on LS-174T using a micropipette
F
Gray value
Width 130 nm
Width 142 nm
0
100
200
300
400
Distance (nm)

Fig. 4. Trypsin treatment to improve CAR T-cell/CRC cell interaction. (A) Cartoon shows trypsin treatment on 48 hrs seeded LS-174T monolayer using a micropipette to dissociate cells followed by CAR T-cell addition and epifluorescence calcium imaging. Calcium flux traces of (B) Jurkat CAR and (C) primary CAR T-cells on trypsin treated LS-174T (orange) and RKO (olive) monolayers. Comparison of (D) calcium flux traces and (E) CEACAM5 mapping before and after trypsin treatment on LS-174T monolayer. Anti-CEACAM5 antibody was added after trypsin treatment and CEACAM5s were imaged every 20 mins for one hour. Scale bars are 10 μm. (F) 2D resPAINT images of LS-174T cell glycocalyx in the presence of trypsin and corresponding line profiles. Scale bars are 1 μm. For each condition of B-D, results are representative of 5-7 (n = 5-7) and 3-4 (n =3-4) FOVs of Jurkat CAR T-cell/CRC and primary CAR T-cell/CRC interactions, respectively. For E and F, we repeated experiments for 4 (n = 4) and 3 (n =3) times, respectively.